Synthesis of highly non-stoichiometric Cu_2ZnSnS_4 nanoparticles with tunable bandgaps

Yasushi Hamanaka, Wataru Oyaizu, Masanari Kawase

Department of Materials Science and Engineering, Nagoya Institute of Technology, Nagoya 466-8555, Japan

Toshihiro Kuzuya

College of Design and Manufacturing Technology, Muroran Institute of Technology, Muroran 050-8585, Japan

Corresponding author: Yasushi Hamanaka

E-mail: hamanaka@nitech.ac.jp

Tel: +81-52-735-7197

Fax: +81-52-735-7680

Acknowledgments

This work was partly supported by the Nanotechnology Platform Program (Molecule and Material Synthesis) of the Ministry of Education, Culture, Sports, Science and Technology (MEXT), Japan as well as JSPS KAKENHI Grant Number 26400316 and 25420785. PLE spectra were measured at Institute for Molecular Science, Okazaki, Japan. We would like to acknowledge Prof. T. Hihara for his assistance in TEM observations.

Abstract

Non-stoichiometric Cu_2ZnSnS_4 nanoparticles with average diameters of 4–15 nm and quasi polyhedral shape were successfully synthesized by a colloidal method. We found that a non-stoichiometric composition of Zn to Cu in Cu_2ZnSnS_4 nanoparticles yielded a correlation where Zn content increased with a decrease in Cu content, suggesting formation of lattice defects relating to Cu and Zn, such as a Cu vacancy (V_{Cu}), antisite with Zn replacing Cu (Zn_{Cu}) and/or defect cluster of V_{Cu} and Zn_{Cu}. The bandgap energy of Cu_2ZnSnS_4 nanoparticles systematically varies between 1.56 and 1.83 eV depending on the composition ratios of Cu and Zn, resulting in a wider bandgap for Cu-deficient Cu_2ZnSnS_4 nanoparticles. These characteristics can be ascribed to the modification in electronic band structures due to formation of V_{Cu} and Zn_{Cu} on the analogy of ternary copper chalcogenide, chalcopyrite $CuInSe_2$, in which top of the valence band shifts downward with decreasing Cu contents, because much like the structure of $CuInSe_2$ the top of the valence band is composed of a Cu 3*d* orbital in Cu_2ZnSnS_4.

Keywords: CZTS nanoparticle, bandgap engineering, non-stoichiometric composition, photovoltaic materials

Introduction

Presently, Cu_2ZnSnS_4 (CZTS) is the most promising candidate for environmentally and economically compatible photovoltaic materials, which can achieve high-efficiency energy conversion (Siebentritt et al. 2012; Ramasamy et al. 2012). CZTS consists of low-toxicity and earth-abundant elements only, unlike other novel photovoltaic materials with higher conversion efficiencies such as CdTe, $Cu(InGa)Se_2$ and lead-halide perovskite. The high absorption coefficient of ~10^4 cm^{-1} and a bandgap of ~1.5 eV indicate that CZTS is one of the ideal semiconductors available to thin-film solar-cell absorbers (Ito et al. 1988). These advantages have accelerated research on both fundamental material properties and solar-cell applications of CZTS (Siebentritt et al. 2012; Ramasamy et al. 2012).

Among the various methods utilized for synthesizing semiconductor thin films, a solution-based process using 'nanoparticle ink', in which semiconductor nanoparticles dispersed in solvent are painted or printed on substrates followed by a sintering process, is a strong candidate for low-cost processing methods for the production of photovoltaic devices (Guo et al. 2009; Genovese et al. 2012; McLeod et al. 2015). In addition, semiconductor quantum dots (QDs), which are very small semiconductor nanoparticles less than the exciton Bohr radius, have also attracted much attention because of unique electronic and optical properties that originate from the quantum confinement effect of carriers (Nalwa 2000). From such characteristics, QDs have attracted considerable attention as key materials not only for various light-emission devices but also for the next-generation photovoltaic materials. This is because extremely high efficiencies exceeding the Shockley–Queisser power conversion limit are theoretically predicted in QD solar cells which can operate based on unconventional mechanisms such as intermediate band structures, multiple exciton generation, etc (Nozik 2010).

On the basis of these aspects, studies on synthesizing size-controlled colloidal CZTS nanoparticles have been actively conducted, and the optical and electronic properties of these nanoparticles have been investigated (Guo et al. 2009; Riha et al. 2009; Steinhagen et al. 2009; Dai et al. 2010; Shavel et al. 2012; Pundsack et al. 2013; Fan et al. 2014). CZTS nanoparticles with diameters less than ~3 nm exhibit apparent enlargement in bandgap energy because of the quantum confinement effect of carriers, where it increases from ~1.5 eV for bulks up to ~1.8 eV for 2 nm (Khare et al. 2011; Liu et al. 2013; Nishi et al. 2014). It has been also reported that the bandgap of CZTS nanoparticles can be controlled over a wide range, depending on elemental composition ratios in comparison with the quantum size effects. Compositions of the cationic elements in CZTS nanoparticles (Cu, Zn and Sn) were investigated in the preceding studies (Nishi et al. 2013; Chen et al. 2014) and are plotted as a ternary diagram in Fig. 1. As shown in Fig. 1, previously reported compositions were limited to non-stoichiometric regions corresponding to the alloy between Cu_2SnS_3 (CTS) and ZnS (Chen et al. 2014), or the narrow region centered on the stoichiometry (Nishi et al. 2013).

Depending on the ratio between CTS and ZnS, the bandgap energy varied between ~3.1 eV for ZnS and < 1.5 eV for CTS (Nishi et al. 2013; Chen et al. 2014). Such behavior is analogous to the bandgap change observed in many mixed crystal semiconductors and empirically explained by Vegard's law in bandgaps (Basu 1997). Altering the mixing ratio of two semiconductor species is the most common procedure of engineering to control the bandgap of semiconductors. However, as for CZTS, the mechanism for the bandgap changes dependent on cation compositions has not been elucidated.

In this study, we have synthesized non-stoichiometric CZTS nanoparticles with the cation composition ratios deviating from the CTS–ZnS alloys in order to examine the key elements that determine the bandgap energy of non-stoichiometric CZTS. It was found that the bandgap energies vary depending on the contents of Cu and Zn but not on the contents of Sn. By the systematic investigation, we have identified Cu as a key element determining the bandgap energies. These observations provide a novel method for manufacturing the bandgap energy of CZTS nanoparticles which can contribute improvement of photovoltaic conversion efficiency of CZTS-based solar-cells.

Experimental

Non-stoichiometric CZTS nanoparticles with surface passivated by 1-dodecanethiol (1-DT, $C_{12}H_{25}SH$) ligands were synthesized by the reaction between metal sources and a sulfur source in the solution phase. Copper acetate, zinc acetate and tin chloride were mixed with dioctylamine in a three-neck flask. The mixture was kept at 363 K in an argon gas atmosphere for 30 min, and then heated. When the temperature of the solution reached 423 K, sulfur powder dissolved in 1-DT was injected. After injection, the solution was heated up to 503 K and kept intact for 120 min, and then cooled to room temperature. Black-colored colloidal solution was obtained. The crude nanoparticles were thoroughly washed by repeated precipitation with an addition of ethanol followed by centrifugation. Finally, the purified nanoparticles were dispersed in hexane and drop-casted on quartz or silicon substrates. To achieve Cu-poor compositions, the molar ratios of Cu, Zn and Sn ions in the starting reagents were varied from the stoichiometric composition of CZTS, i.e. Cu:Zn:Sn = 2:1:1, to highly non-stoichiometric Cu:Zn:Sn = 2:15:15, keeping equivalent total amounts of Zn, Sn and S ions in the reagents. In other words, the molar ratios of Cu to the total amount of metals, $x = [Cu]/([Cu] + [Zn] + [Sn])$, were changed between 1/2 and 1/16.

The elemental compositions of the synthesized nanoparticles were examined using X-ray photoelectron spectroscopy (XPS) measured by ULVAC PHI5000. Before the XPS measurements, surface cleaning of the nanoparticles deposited on silicon substrates was conducted by C_{60} ion beam sputtering. The XPS spectra of Cu 2*p*, Zn 2*p*, Sn 3*d*, S 2*p* and C 1*s* electrons were measured and analyzed by a deconvolution technique. Transmission electron microscopy (TEM) of individual nanoparticles were performed by Hitachi HF2000 and JEOL JEM2100F. The crystalline structures of the nanoparticles were investigated by X-ray diffraction (XRD) and Raman spectroscopy. XRD patterns were measured by a powder diffractometer using Cu-Kα radiation (Mac Science High Quality XG). Raman spectra were obtained by excitation at 532 nm using JASCO NRS-3300 Raman spectrometer. To investigate optical bandgap energies of nanoparticles, photoluminescence excitation (PLE) spectra were measured using a Horiba SPEX Fluorolog3 spectrofluorometer equipped with a near-infrared photomultiplier tube.

Results and discussion

Reaction scheme

In this procedure, we employed the conventional metathesis reaction between metal complex and sulfur complex. Sulfur-1-DT (RSH) complex was decomposed to H_2S, which react with metal complex to form chalcogenide. The composition of CZTS NPs is decided by formation rates of Cu_2S, ZnS, and SnS_2, which differ from each other. On the other hand, high ionic conductivity of chalcogenides may lead to the cation exchange process. Under equilibrium condition, the chemical composition (Cu:Zn:Sn) of CZTS NPs are decided by the stability of metal complexes in solution phase (Kuzuya et al. 2012).

Elemental compositions

Figure 2 shows the XPS spectra obtained for nanoparticles synthesized from starting compositions of x = 1/10 (sample F, Cu:Zn:Sn = 2:9:9). Characteristic peaks of Cu, Zn, Sn, S and C atoms are present in these spectra. The peaks of Cu $2p_{3/2}$ (932 eV), Cu $2p_{1/2}$ (952 eV), Zn $2p_{3/2}$ (1022 eV), Zn $2p_{1/2}$ (1045 eV), Sn $3d_{5/2}$ (486 eV), Sn $3d_{3/2}$ (495 eV), S $2p$ (161–165 eV) and C $1s$ (284.8 eV) were observed. A shoulder peak located at the high-energy side of the Sn $3d_{3/2}$ peak (Fig. 2 (c)) was assigned to an Auger electron peak of Zn (Wagner et al. 1979). All of the peaks for Cu, Zn and Sn, except for Sn $3d_{3/2}$ and an Auger peak, exhibit asymmetrical features because of a shoulder on the high-energy side of each peak. Such spectral features suggest that additional weak peaks exist there. These main and additional peaks could be deconvoluted by fitting analysis. In this analysis, we adopted a Voigt function for representing the peak profiles. As shown in Fig. 2 (a)–(c), each asymmetric peak was well fitted by this procedure. Peak energies of the weak components were estimated to be 1–2 eV higher than the main peaks. The main peaks appeared on a similar energy position to those reported for bulk CZTS (Bär et al. 2011); hence, these were identified as the signals of Cu, Zn and Sn belonging to the nanoparticles. Weak components may originate in Cu, Zn and Sn from some impurities or secondary phases; however, we cannot identify these species.

It is well known that the S 2*p* peak splits into two separate peaks with a distance of 1.2 eV and an intensity ratio of 2:1, which originate in S $2p_{3/2}$ and S $2p_{1/2}$ electrons (Wagner et al. 1979). However, measured spectrum of S 2*p* electrons (Fig. 2(d)) exhibited complicated features, suggesting that several overlapping peaks exist in this region. Taking into account these characteristics of the S 2*p* spectrum, we also analyzed S 2*p* spectra by the same deconvolution method adopted to the metal peaks as described above. The spectral shape of the S 2*p* was successfully reproduced by two sets of S $2p_{3/2}$ and S $2p_{1/2}$ peaks. This estimation is reasonable because there exist two types of S atoms in these nanoparticles; S in the nanoparticle bodies and 1-DT ligands. On the basis of the peak energies, we can identify that the low- and high-energy peak sets correspond to the S 2*p* electrons in S bonded with metals (dashed curves in Fig. 2(d)) and S bonded with C in alkyl chains of 1-DT (dot-dashed curves in Fig. 2(d)), respectively (Caster et al. 1996; Xu et al. 1998; Cruz et al. 2003; Krylova and Andrulevičius 2009). This conclusion is supported by the XPS spectrum of C 1*s* electrons shown in Fig. 2 (e); this may be attributed to the 1-DT ligands, in which two types of C exist, bound and non-bound S. The C 1*s* peak could be also deconvoluted into two components, the main peak at 284.8 eV and the weak peak at 286.07 eV. This result indicates that the weak component is ascribed to C atoms bonded with S, and the main peak is ascribed to C not bonded with S. Consequently, we conclude that the S 2*p* peaks appearing in high-energy and low-energy regions are because of S belonging to 1-DT ligands and nanoparticles, respectively. Therefore, an elemental composition of nanoparticles can be deduced from integrated intensities of Cu 2*p*, Zn 2*p*, Sn 3*d* and S 2*p* peaks originated in the nanoparticles, considering the relative sensitivity factors of each element in XPS measurements. In this way, we successfully estimated accurate values of elemental compositions of the nanoparticles by separating them from the same elements in impurities and secondary phases. The composition ratio of the sample F was determined to be Cu:Zn:Sn:S = 1.03:1.90:0.94:4.13. Cu and Zn contents are half and nearly twice the stoichiometric values, respectively, whereas Sn and S contents are close to a stoichiometric ratio.

Elemental compositions were also evaluated for other nanoparticle samples synthesized in this study. The results are summarized in Table 1 and cation compositions are plotted in the ternary diagram shown in Fig. 1. As shown in the ternary diagram, the cation composition ratios of these nanoparticles are different from the previously reported CTS–ZnS-alloyed nanoparticles (Nishi et al. 2013; Chen et al. 2014). The ratio of Cu:Zn:Sn varies between near-stoichiometric 2.08:1.34:1.31 (sample A) and highly non-stoichiometric 1.08:2.49:0.83 (sample E), where the Zn content increases with a decrease of Cu content. This tendency suggests that Cu atoms were substituted with Zn under the Cu-poor condition, indicating that the antisite with Zn replacing Cu (Zn_{Cu}) as well as the Cu vacancy (V_{Cu}) were possibly formed. The antisite Zn_{Cu} can be easily formed because Cu^+ and Zn^{2+} with a coordination number of 4 have identical ionic radii of 0.6 Å (Shannon 1976). Such an assumption is also supported by the recent theoretical prediction that V_{Cu} and V_{Cu} + Zn_{Cu} defect clusters in CZTS have relatively low formation energies (Chen et al. 2010).

Structural investigations

Typical TEM images of CZTS nanoparticles are depicted in Fig. 3 (a) and (c) for near-stoichiometric (sample A) and non-stoichiometric (sample F) compositions, respectively. These nanoparticles exhibit quasi polyhedral shapes and approximately ~7 nm (A) and ~5 nm (F) in average diameters. Electron diffraction patterns of the corresponding nanoparticles are shown in Fig. 3 (b) and (d). Three diffraction rings were observed for both of the nanoparticles, which indicate that the nanoparticles are well crystalized. The interplanar spacings estimated from the diffraction rings were about 3.1, 1.9, and 1.6 Å in both cases. These values are in accordance with the (112), (220), and (312) planes of kesterite CZTS, respectively (Joint Committee on Powder Diffraction Standards (JCPDS) 075-4122). TEM observation of any other compositions showed that nanoparticle shapes were near polyhedral and their average diameters varied from ~4 to ~15 nm independent of composition of starting reagents (Electronic Supplementary Material). Average diameters above ~4 nm are larger than the diameter for an enlargement in the bandgap because of the quantum confinement effect, suggesting the bulk-like electronic states of nanoparticles prepared in this study (Khare et al. 2011; Liu et al. 2013; Nishi et al. 2014). However, very small particle size and low contrast of TEM images make it difficult to estimate accurate size of individual nanoparticles. Therefore, crystallite size of nanoparticles were also investigated by analyzing XRD peak width using the Scherrer equation.

XRD patterns of each nanoparticle sample deposited on quartz substrates are shown in Fig. 4 in conjunction with the JCPDS data of CZTS, cubic ZnS and cubic CTS. Diffraction patterns characterized by three intense peaks appearing around $2\theta = 28°$, 47° and 57° were observed for many compositions. Broad diffraction peaks around 20° were because of quartz substrates. Many sharp peaks below $2\theta = 30°$ observed in the sample C and weak structures at $2\theta = 32°$ and 49° in several samples were most likely from residual organic impurities which can be ascribed to the copper-thiolates (Espinet et al. 1999). The position and intensity ratio of the main diffraction peaks closely match those reported for CZTS bulk crystals (Nagaoka et al. 2012) and films (Washio et al. 2011), as well as the JCPDS data. This indicates that fundamental crystalline structures of CZTS, including lattice constants, are maintained despite highly non-stoichiometric compositions, which is consistent with the electron diffraction patterns. However, it is difficult to distinguish the diffraction patterns of CZTS from other compounds such as cubic ZnS and CTS, which are possibly produced as secondary phases. Thus, Raman spectra have been often used for CZTS characterization (Khare et al. 2011; Nagaoka et al. 2012; Shavel et al. 2012; Liu et al. 2013; Nishi et al. 2013; Chen et al. 2014).

Figure 5 shows the Raman spectra of the same nanoparticles deposited on silicon substrates. Frequencies of the

Raman spectra were calibrated using the longitudinal optical (LO) phonon peak of the silicon substrates. The Raman peaks were observed at 327–335 cm^{-1}, which are closely match previously reported values for the A_1 mode of bulk CZTS, and are different from the characteristic peaks of ZnS (275, 350 cm^{-1}) (Serrano et al. 2004) and CTS (303, 355 cm^{-1}) (Fernandes et al. 2010). However, peak frequencies are slightly lower than the A_1 peak reported for stoichiometric single crystals, 336 cm^{-1} (Levcenko et al. 2012) or 338 cm^{-1} (Nagaoka et al. 2012). Grossberg *et al.* (2012) observed the Raman band at the frequency similar to our results and ascribed it to disordered kesterite, where disorder of the cation position exists in the Cu–Zn layer. Such disordered CZTS were actually identified by neutron scattering and the presence of anti-sites of Zn_{Cu} and Cu_{Zn} were reported (Schorr 2011). The low-frequency Raman peak at 331 cm^{-1} was reported for CZTS films evaporated at low substrate temperatures and also ascribed to the structural disorder in a cationic sub-lattice (Caballero et al. 2014). Thus, our Raman results suggest disordering at the Cu and Zn sites in the Cu–Zn layer because of non-stoichiometric compositions of Cu-poor and Zn-rich conditions. We can see no pronounced difference in Raman frequencies in spite of the wide variations of Cu and Zn compositions. The following point can be considered as the reason. The A_1 mode is a pure anion mode in which only S atoms vibrate; hence, its frequency is less affected by composition variations of other cation atoms (Khare et al. 2012). Consequently from this analysis, the nanoparticles synthesized in this study could be identified as CZTS nanoparticles with high non-stoichiometric Cu and Zn compositions. However, as can be seen in Fig. 5, the Raman spectrum of the sample H exhibited the hump on the frequencies corresponding to the phonon mode of ZnS (LO) and CTS, suggesting the formation of secondary phase of ZnS (and CTS) which could not be identified by XPS and XRD.

The lattice constants of samples A–H calculated from the (112), (220) and (312) peaks of the XRD patterns are shown in Table 1. The lattice constants are 5.406–5.441 Å and 11.061–11.425 Å for *a*- and *c*-axis, respectively. There is no systematic dependence on the elemental compositions in these values. The crystallite size estimated from full width at half maximum (FWHM) of the (220) and (312) diffraction peaks by the Scherrer equation is also shown in Table 1. The crystallite sizes are 4–5 nm which are equivalent to or slightly smaller compared with the average diameters of nanoparticles measured by TEM. These results are not contradict the TEM observation where nanoparticle diameters are 4–15 nm.

Optoelectronic properties

Investigation of optoelectronic properties of non-stoichiometric CZTS nanoparticles dependent on the elemental compositions was conducted. It is well documented that the bandgap energy of a semiconductor can usually be estimated from the optical absorption spectrum by analyzing the spectral shape around an absorption edge (Yu and

Cardona 2010). However, nanoparticle samples prepared in this study were not suitable for absorption spectroscopy because of strong light scattering because of rough surfaces. The PLE spectrum is approximately equivalent to the absorption spectrum of the sample (Yu and Cardona 2010). Thus, we estimated bandgap energies E_g of the non-stoichiometric CZTS nanoparticles using the PLE spectra instead of the absorption spectra. In direct bandgap semiconductors, an absorption coefficient α near the absorption edge can be expressed as the following formula (Yu and Cardona 2010),

$$\alpha = A\frac{\left(h\nu - E_g\right)^{1/2}}{h\nu} \tag{1}$$

Here, A, h and ν are a proportional constant, Planck's constant and frequency of light, respectively. E_g can be estimated as a zero-crossing energy from the plot of $(\alpha h\nu)^2$ against $h\nu$. In this study, α was replaced by the intensity of PLE spectrum I_{PLE} for analysis of E_g because I_{PLE} is proportional to α. The PLE spectra of the CZTS nanoparticles were measured by monitoring intensities of PL spectra peaked at 1–1.2 eV. Figure 6 shows the PLE spectra of the CZTS nanoparticles displayed in the plot of $(I_{\mathrm{PLE}}\,h\nu)^2$ versus $h\nu$. We could not obtain clear PLE spectra for some compositions (sample B and C) because of weak emission. PLE spectrum of the sample H is not shown here because of possible presence of the secondary phase detected by Raman measurement. As shown in Fig. 6, rising edge energies of the PLE spectra are different depending on the compositions of nanoparticles, which indicates that the E_g is dependent on the elemental compositions. The E_g values were estimated from the plot shown in Fig. 6 by extrapolating the linear part of each spectrum.

Estimated E_g values are shown in Table 1 and plotted versus Cu, Zn and Sn content ratios to all cations, respectively, in Fig. 7, with E_g previously reported for non-stoichiometric CZTS nanoparticles with compositions of a $\mathrm{CTS}_x(\mathrm{ZnS})_{1-x}$ alloy (Nishi et al. 2013; Chen et al. 2014). The results show that E_g of the CZTS nanoparticles with Cu:Zn:Sn = 1.58:1.02:1 is minimal at 1.56 eV, which is equivalent to that of stoichiometric CZTS, and that of highly non-stoichiometric Cu:Zn:Sn = 1.3:3:1 is 1.83 eV. The E_g values are strongly correlated with the content ratios of both Cu and Zn. E_g increases with a decrease in Cu composition and an increase in Zn composition. Such behaviors are also found in the former $\mathrm{CTS}_x(\mathrm{ZnS})_{1-x}$-alloyed nanoparticles (Nishi et al. 2013; Chen et al. 2014). However, we cannot find apparent Sn-composition dependence, although clear dependences were found in alloyed nanoparticles. Correlation coefficients between E_g and the Cu composition ratio as well as between E_g and the Zn composition ratio were estimated to be −0.97 and 0.86, respectively. These are much larger than the coefficient of −0.52 derived for Sn composition. These results suggest that Cu and Zn compositions are key parameters in determining E_g of the CZTS nanoparticles.

The bandgap widening similar to the non-stoichiometric CZTS nanoparticles was reported in other non-stoichiometric copper chalcogenides, chalcopyrite $CuInSe_2$ (CISe), with Cu-poor composition (Philip and Pradeep 2003). In CISe, the bandgap change was explained in terms of formation of $2V_{Cu} + In_{Cu}$ defect clusters and modification in the electronic band structure was associated with these defects (Zhang et al. 1998). The LDA calculation indicated that valence band maximum (VBM) of CISe is composed of hybridized states between Cu 3*d* and Se 4*p* orbitals and there exists a *p*–*d* repulsion gap, which separates the upper anti-bonding states and lower bonding states. Increases in the number of V_{Cu} and In_{Cu} weakens the *p*–*d* hybridization, resulting in weak *p*–*d* repulsion and reduction of the repulsion gap. Thus, the bandgap increases as a result of the down-shift of the top of VBM because it is composed of the anti-bonding states. Like the Cu chalcopyrite, the VBM of CZTS is composed of hybridized states between Cu 3*d* and S 3*p* orbitals and a *p*–*d* repulsion gap exists (Chen et al. 2013). Therefore, the hybridization will be weakened when V_{Cu} is formed or Cu is substituted with other cation atoms. In such a situation, the same as in CISe, the *p*–*d* repulsion gap is decreased; hence, the bandgap widens. Structural analysis in this study suggested that the V_{Cu} and/or $V_{Cu} + Zn_{Cu}$ defect clusters could be created in our non-stoichiometric CZTS nanoparticles. Such defects may weaken the hybridization between Cu 3*d* and S 3*p*. Therefore, E_g values of CZTS nanoparticles depend strongly on the composition ratios of both Cu and Zn, but Sn-composition dependence is much weaker.

Conclusions

We synthesized CZTS nanoparticles with diameters of 4–15 nm and large non-stoichiometric cation compositions by the colloidal method. Bandgap energies of non-stoichiometric CZTS nanoparticles predominantly depends on the contents of Cu and Zn in nanoparticles; an increase in energy with a decrease in Cu composition and an increase in Zn composition. Such tendencies may be ascribed to formation of V_{Cu} and/or $V_{Cu} + Zn_{Cu}$ defect clusters on the analogy of Cu-poor CISe, which can weaken the Cu 3*d*–S 3*p* hybridization in the VBM and cause a down-shift of the VBM. This approach presents a potential technique for the bandgap engineering of CZTS nanoparticles, which enables precise tuning of the absorption wavelength while contributing to advancement in photovoltaic technology.

Compliance with Ethical Standards

Funding: This study was funded by the Japan Society for the Promotion of Science (grant numbers 26400316 and 25420785).

Conflict of interest: The authors declare that they have no conflict of interest.

References

Basu PK (1997) Theory of Optical Processes in Semiconductors Bulk and Microstructures. Oxford, Clarendon

Bär M, Schubert B-A, Marsen B, Krause S, Pookpanratana S, Unold T, Weinhardt L, Heske C, Schock H–W (2011) Native oxidation and Cu-poor surface structure of thin film Cu_2ZnSnS_4 solar cell absorbers. Appl. Phys. Lett. 99(11):112103-1–112103-3

Caballero R, Garcia-Llamas E, Merino JM, León M, Babichuk I, Dzhagan V, Strelchuk V, Valakh M (2014) Non-stoichiometry effect and disorder in Cu_2ZnSnS_4 thin films obtained by flash evaporation: Raman scattering investigation. Acta Mater. 65:412–417

Castner DG, Hinds K, Grainger DW (1996) X-ray photoelectron spectroscopy sulfur 2p study of organic thiol and disulphide binding interactions with gold surfaces. Langmuir 12(21):5083–5086

Chen S, Yang J, Gong XG, Walsh A, Wei S-H (2010) Intrinsic point defects and defect complexes in the quaternary kesterite semiconductor Cu_2ZnSnS_4. Phys. Rev. B 81(24):245204-1–245204-10

Chen S, Walsh A, Gong X, Wei S-H (2013) Classification of lattice defects in the kesterite Cu_2ZnSnS_4 and $Cu_2ZnSnSe_4$ earth-abundant solar cell absorbers. Adv. Mater. 25(11):1522–1539

Chen Y, Chuang C, Lin K, Shen S, McCleese C, Guo L, Burda C (2014) Synthesis and photoelectrochemical properties of $(Cu_2Sn)_xZn_{3(1-x)}S_3$ nanocrystal films. J. Phys. Chem. C 118(22):11954–11963

Cruz M, Morales J, Espinos JP, Sanz J (2003) XRD, XPS and ^{119}Sn NMR study of tin sulfides obtained by using chemical vapour transport methods. J. Solid State Chem. 175(2):359–365

Dai P, Shen X, Lin Z, Feng Z, Xu H, Zhan J (2010) Band-gap tunable $(Cu_2Sn)_{x/3}Zn_{1-x}S$ nanoparticles for solar cells. Chem. Commun. 46(31):5749–5751

Espinet P, Lequerica MC, Martín-Alvarez JM (1999) Synthesis, structural characterization and mesogenic behavior of copper (I) n-alkylthiolates. Chem. Eur. J. 5(7):1982-1986

Fan F, Wu L, Yu S (2014) Energetic I-III-VI_2 and I_2-II-IV-VI_4 nanocrystals: synthesis, photovoltaic and thermoelectric applications. Energy Environ. Sci. 7(1):190–208

Fernandes PA, Salomé PMP, da Cunha AF (2010) A study of ternary Cu_2SnS_3 and Cu_3SnS_4 thin films prepared by sulfurizing stacked metal precursors. J. Phys. D: Appl. Phys. 43(21):215403-1–215403-11

Genovese MP, Lightcap IV, Kamat PV (2012) Sun-believable solar paint. A transformative one-step approach for designing nanocrystalline solar cells. ACS Nano 6(1):865–872

Grossberg M, Krustok J, Raudoja J, Raadik T (2012) The role of structural properties on deep defect states in Cu_2ZnSnS_4 studied by photoluminescence spectroscopy. Appl. Phys. Lett. 101(10):102102-1–102102-4

Guo Q, Hillhouse HW, Agrawal R (2009) Synthesis of Cu_2ZnSnS_4 nanocrystal ink and its use for solar cells. J. Am. Chem. Soc. 131(33):11672–11673

Ito K, Nakazawa T (1988) Electrical and optical properties of stannite-type quaternary semiconductor thin films. Jpn. J. Appl. Phys. 27(11):2094–2097

Khare A, Wills AW, Ammerman LM, Norris DJ, Aydil ES (2011) Size control and quantum confinement in Cu_2ZnSnS_4 nanocrystals. Chem. Commun. 47(42):11721–11723

Khare A, Himmetoglu B, Johnson M, Norris DJ, Cococcioni M, Aydil ES (2012) Calculation of the lattice dynamics and Raman spectra of copper zinc tin chalcogenides and comparison to experiments. J. Appl. Phys. 111(8):083707-1–083707-9

Krylova V, Andrulevičius M (2009) Optical XPS and XRD studies of semiconducting copper sulphide layers on a polyamide film. Int. J. Photoenergy, 2009(3):304308-1–304308-8

Kuzuya T, Hamanaka Y, Itoh K, Kino T, Sumiyama K, Fukunaka Y, Hirai S (2012) Phase control and its mechanism of $CuInS_2$ nanoparticles. J. Colloid Interface Sci. 388(1):137–143.

Levcenko S, Tezlevan VE, Asushanov E, Schorr S, Unold T (2012) Free-to-bound recombination in near stoichiometric Cu_2ZnSnS_4 single crystals. Phys. Rev. B 86(4):045206-1–045206-6

Liu WC, Guo BL, Wu XS, Zhang FM, Mak CL, Wong KH (2013) Facile hydrothermal synthesis of hydrotropic Cu_2ZnSnS_4 nanocrystal quantum dots: band-gap engineering and phonon confinement effect. J. Mater. Chem. A 1(9):3182–3186

Mcleod SM, Hages CJ, Carter NJ, Agrawal R (2015) Synthesis and characterization of 15 % efficient CIGSSe solar cells from nanoparticle inks. Prog. Photovolt: Res. Appl. 23(11):1550–1556

Nagaoka A, Yoshino K, Taniguchi H, Taniyama T, Miyake H (2012) Preparation of Cu_2ZnSnS_4 single crystals from Sn solutions. J. Cryst. Growth 341(1):38–41

Nalwa HS (2000) Nanostructured Materials and Nanotechnology. Academic Press, San Diego

Nishi H, Kuwabata S, Torimoto T (2013) Composition-dependent photoelectrochemical properties of nonstoichiometric Cu_2ZnSnS_4 nanoparticles. J. Phys. Chem. C 117(41):21055–21063

Nishi H, Nagano T, Kuwabata S, Torimoto T (2014) Controllable electronic energy structure of size-controlled Cu_2ZnSnS_4 nanoparticles prepared by a solution-based approach. Phys. Chem. Chem. Phys. 16(2):672–675

Nozik AJ (2010) Nanoscience and nanostructures for photovoltaics and solar fuels. Nano Lett. 10(8):2735–2741

Philip R, Pradeep B (2003) Structural analysis and optical and electrical characterization of the ordered defect compound $CuIn_5Se_8$. Semicond. Sci. Technol. 18(8):768–773

Pundsack TJ, Chernomordik BD, Béland AE, Aydil ES, Blank DA (2013) Excited-state dynamics in CZTS nanocrystals. J. Phys. Chem. Lett. 4(16):2711–2714

Ramasamy K, Malik MA, O'Brien P (2012) Routes to copper zinc tin sulphide Cu_2ZnSnS_4 a potential material for solar cells. Chem. Commun. 48(46):5703–5714

Riha SC, Parkinson BA, Prieto AL (2009) Solution–based synthesis and characterization of Cu_2ZnSnS_4 nanocrystals. J. Am. Chem. Soc. 131(34):12054–12055

Schorr S (2011) The crystal structure of kesterite type compounds: A neutron and X-ray diffraction study. Sol. Energy Mater. Sol. Cells 95(6):1482–1488

Serrano J, Cantarero A, Cardona M, Garro N, Lauck R, Tallman RE, Ritter TM, Weinstein BA (2004) Raman scattering in β-ZnS. Phys. Rev. B 69(1):014301-1–014301-11

Shannon RD (1976) Revised effective ionic radii and systematic studies of interatomic distances in halides and chalcogenides. Acta Cryst. A 32(5):751–767

Shavel A, Cadavid D, Ibáñez M, Carrete A, Cabot A (2012) Continuous production of Cu_2ZnSnS_4 nanocrystals in a flow reactor. J. Am. Chem. Soc. 134(3):1438–1441

Siebentritt S, Schorr S (2012) Kesterites-a challenging material for solar cells. Prog. Photovolt: Res. Appl. 20(5):512–519

Steinhagen C, Panthani MG, Akhavan V, Goodfellow B, Koo B, Korgel BA (2009) Synthesis of Cu_2ZnSnS_4 nanocrystals for use in low-cost photovoltaics. J. Am. Chem. Soc. 131(35):12554–12555

Wagner CD, Riggs WM, Davis LE, Moulder JF, Muilenberg GE (1979) Handbook of X-ray Photoelectron Spectroscopy. Perkin-Elmer Corporation Physical Electronics Division, Eden Prairie

Washio T, Nozaki H, Fukano T, Motohiro T, Jimbo, K, Katagiri H (2011) Analysis of lattice occupancy in kesterite structure of Cu_2ZnSnS_4 films using synchrotron radiation x-ray diffraction. J. Appl. Phys. 110(7):074511-1–074511-4

Xu JF, Ji W, Lin JY, Tang SH, Du YW (1998) Preparation of ZnS nanoparticles by ultrasonic radiation method. Appl. Phys. A 66(6):639–641

Yu PY, Cardona M (2010) Fundamentals of Semiconductors Physics and Materials Properties, fourth ed. Springer, Berlin

Zhang SB, Wei S-H, Zunger A, Katayama-Yoshida H (1998) Defect physics of the $CuInSe_2$ chalcopyrite semiconductor. Phys. Rev. B 57(16):9642–9656

Figure Captions

Fig. 1. Ternary plot of the atomic percentage of Cu, Zn and Sn in the CZTS nanoparticles. ●: this work, □: Nishi et al. (2013), △: Chen et al. (2014)

Fig. 2. XPS spectra of CZTS nanoparticles of sample F: (a) Cu 2*p* (b) Zn 2*p*, (c) Sn 3*d*, (d) S 2*p* and (e) C 1*s*.

Fig. 3. TEM images and electron diffraction patterns of CZTS nanoparticles with near-stoichiometric composition (sample A, (a) and (b)) and non-stoichiometric composition (sample F, (c) and (d)), respectively. Positions of some nanoparticles are marked by the circles in (a) and (c).

Fig. 4. XRD patterns of the CZTS nanoparticles measured using a powder diffractometer with Cu-Kα radiation. For reference, JCPDS data of CZTS, cubic ZnS and cubic CTS are also shown.

Fig. 5. Raman spectra of the CZTS nanoparticles around the A_1 vibrational mode. Thick red bars indicate frequencies and intensities of the Raman bands reported for single crystal CZTS. Thin vertical lines indicate positions of major Raman bands of cubic ZnS and cubic CTS.

Fig. 6. PLE spectra of the CZTS nanoparticles. Vertical axes of the spectra are modified for analysis of bandgap energies. Solid lines represent interpolation of the linear parts of the spectra.

Fig. 7. Relations between the bandgap energies and composition ratios of (a) Cu, (b) Zn and (c) Sn versus whole metallic elements in CZTS nanoparticles. ●: this work, □: Nishi et al. (2013), △: Chen et al. (2014)

Table 1. Composition ratios, crystallite size, lattice constants, and bandgap energies of CZTS nanoparticles.

sample	size (nm)	Cu : Zn : Sn : S	a (Å)	c (Å)	E_g (eV)
A	4.3	2.08 : 1.34 : 1.31 : 3.27	5.410 ± 0.004	11.288 ± 0.084	1.56
B	4.6	1.81 : 1.38 : 1.14 : 3.67	5.408 ± 0.001	11.259 ± 0.014	—
C	5.1	1.66 : 0.81 : 2.13 : 3.40	5.417 ± 0.005	11.072 ± 0.093	—
D	4.0	1.56 : 0.80 : 2.02 : 3.62	5.441 ± 0.000	11.425 ± 0.001	1.64
E	4.8	1.08 : 2.49 : 0.83 : 3.60	5.431 ± 0.001	11.016 ± 0.017	1.83
F	4.0	1.03 : 1.90 : 0.94 : 4.13	5.409 ± 0.012	11.067 ± 0.234	1.77
G	3.8	1.14 : 2.00 : 0.95 : 3.91	5.406 ± 0.008	11.389 ± 0.175	1.82
H*	5.1	1.30 : 2.42 : 1.54 : 2.74	5.429 ± 0.001	11.061 ± 0.026	—

* secondary phases

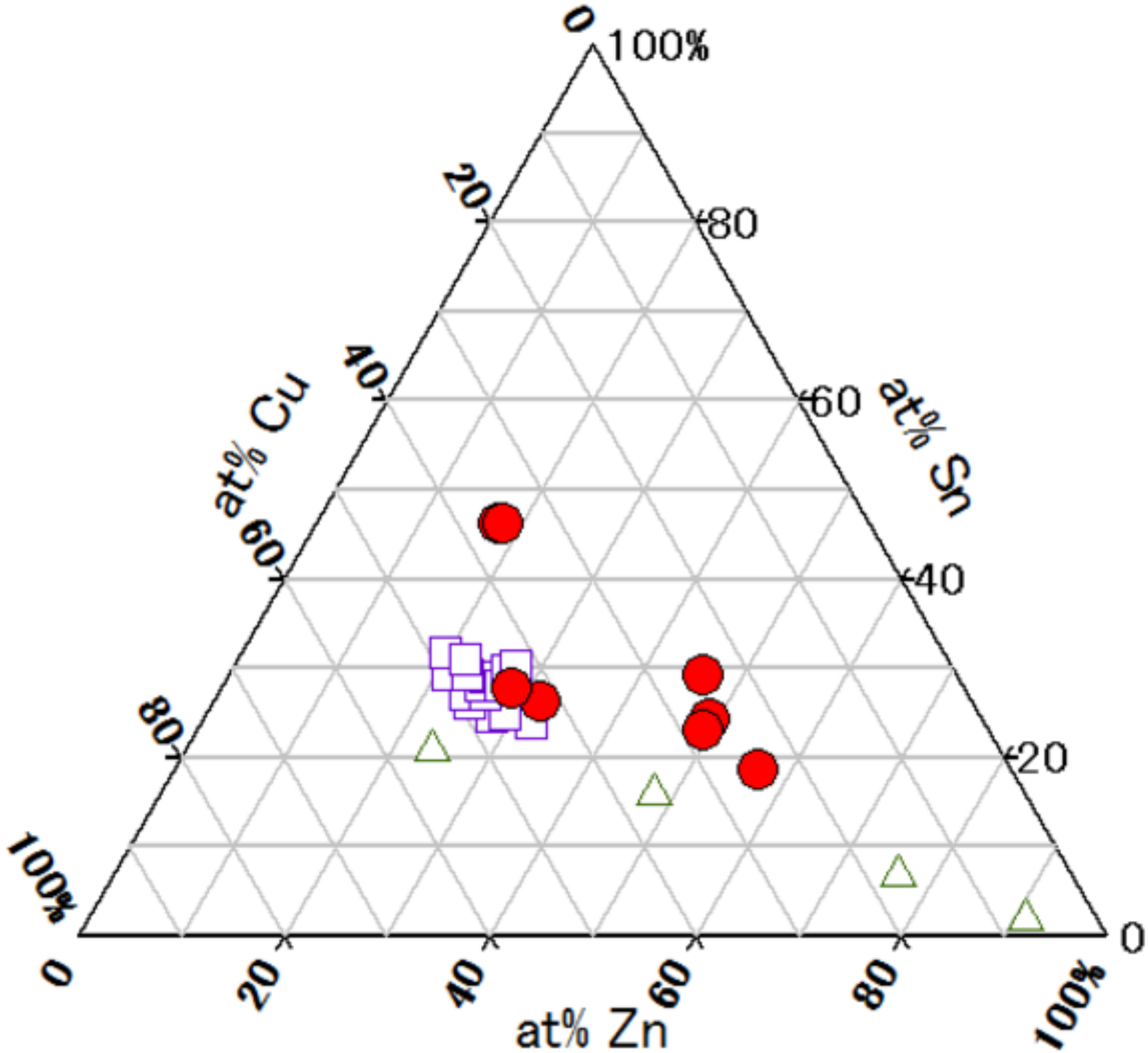
0
100%
20
80
40
60
at% Cu
60
at% Sn
40
80
20
100%
0
0
20
40
60
80
100%
at% Zn

Figure2

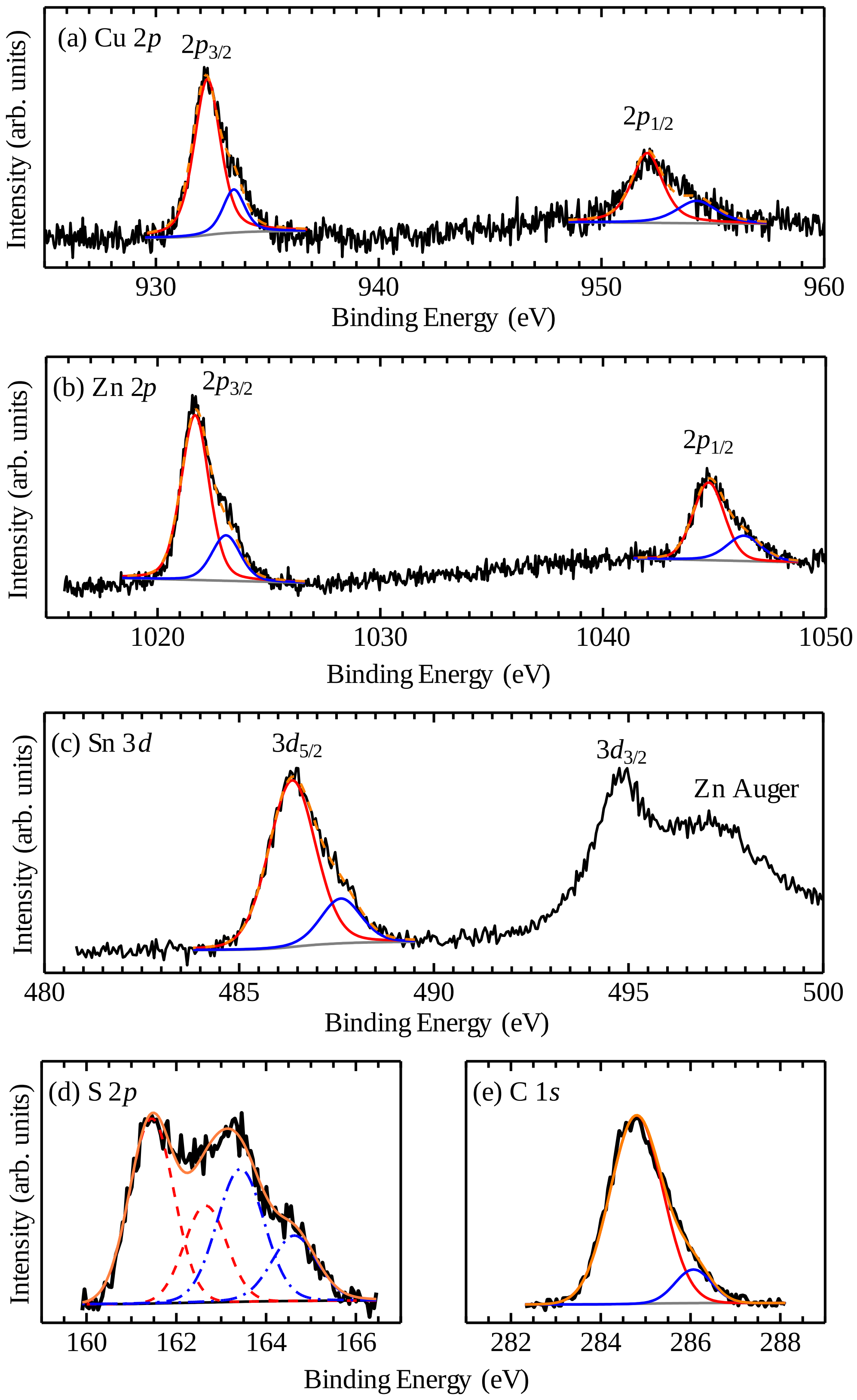
(a) Cu 2p
2p3/2
2p1/2
Intensity (arb. units)
930
940
950
960
Binding Energy (eV)
(b) Zn 2p
2p3/2
2p1/2
Intensity (arb. units)
1020
1030
1040
1050
Binding Energy (eV)
(c) Sn 3d
3d5/2
3d3/2
Zn Auger
Intensity (arb. units)
480
485
490
495
500
Binding Energy (eV)
(d) S 2p
Intensity (arb. units)
160
162
164
166
(e) C 1s
282
284
286
288
Binding Energy (eV)

Figure3

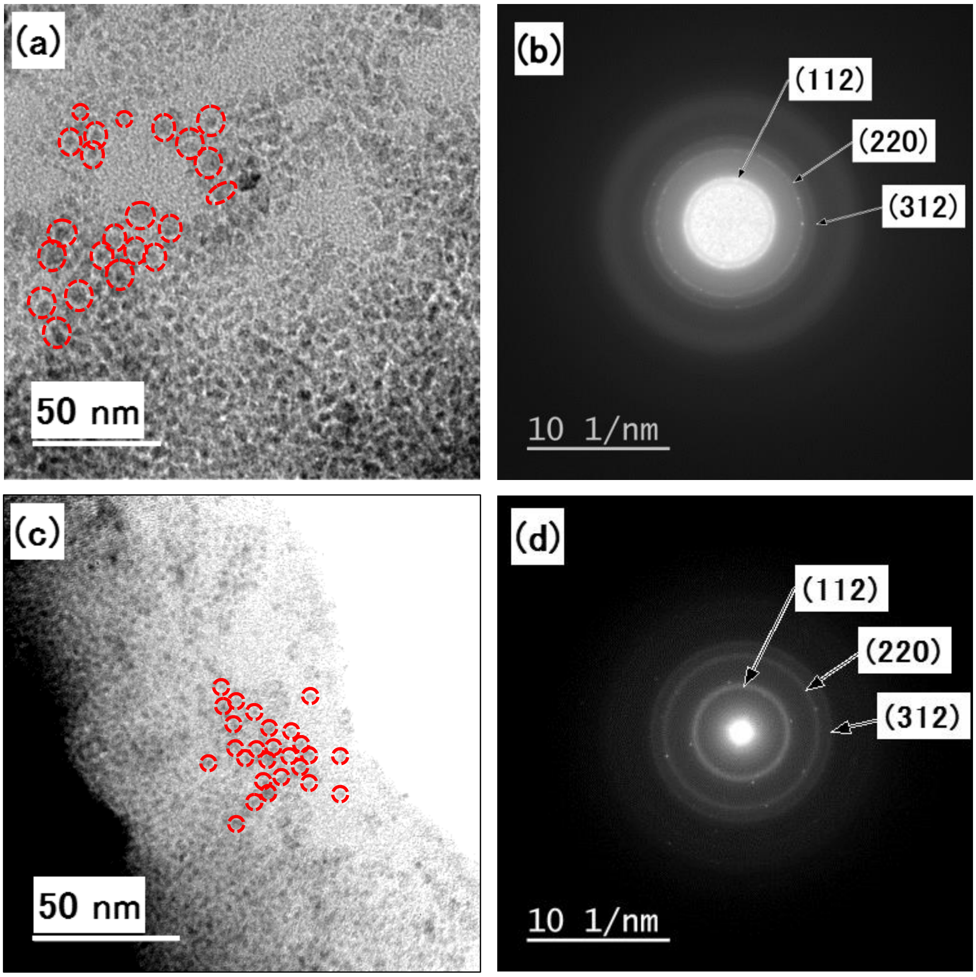

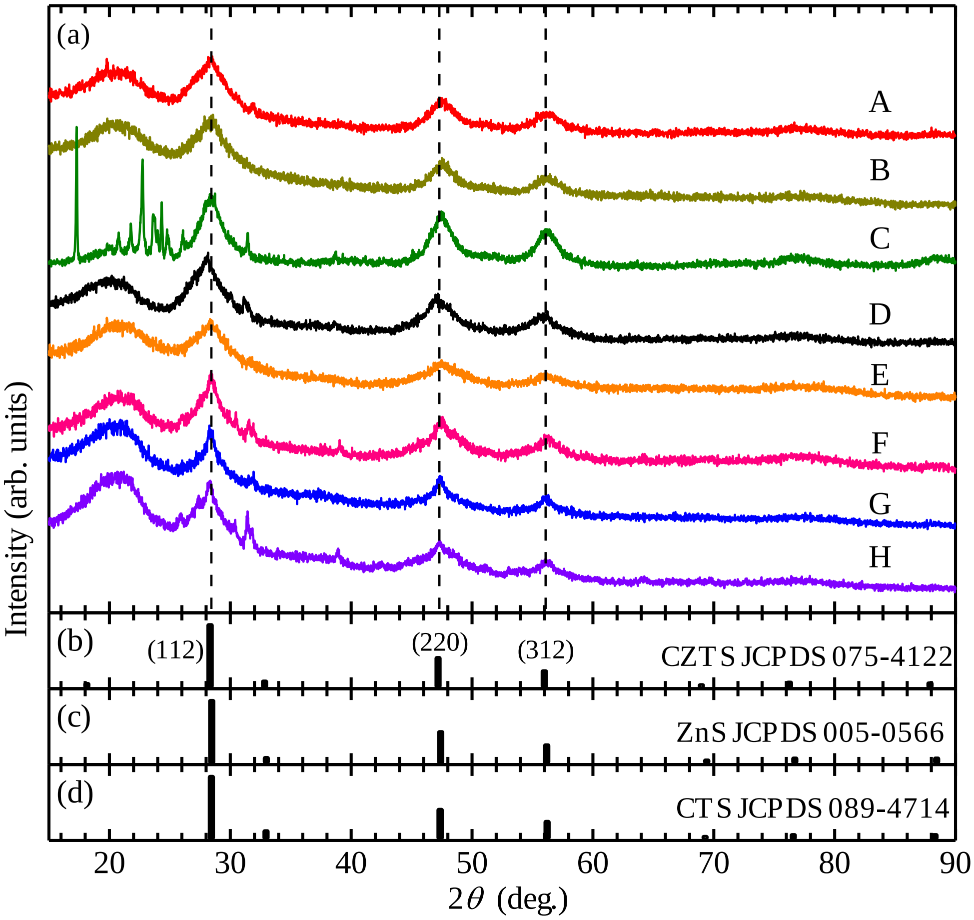
(a)
A
B
C
D
E
F
G
H
Intensity (arb. units)
(b)
(112)
(220)
(312)
CZTS JCPDS 075-4122
(c)
ZnS JCPDS 005-0566
(d)
CTS JCPDS 089-4714
20
30
40
50
60
70
80
90
2θ (deg.)

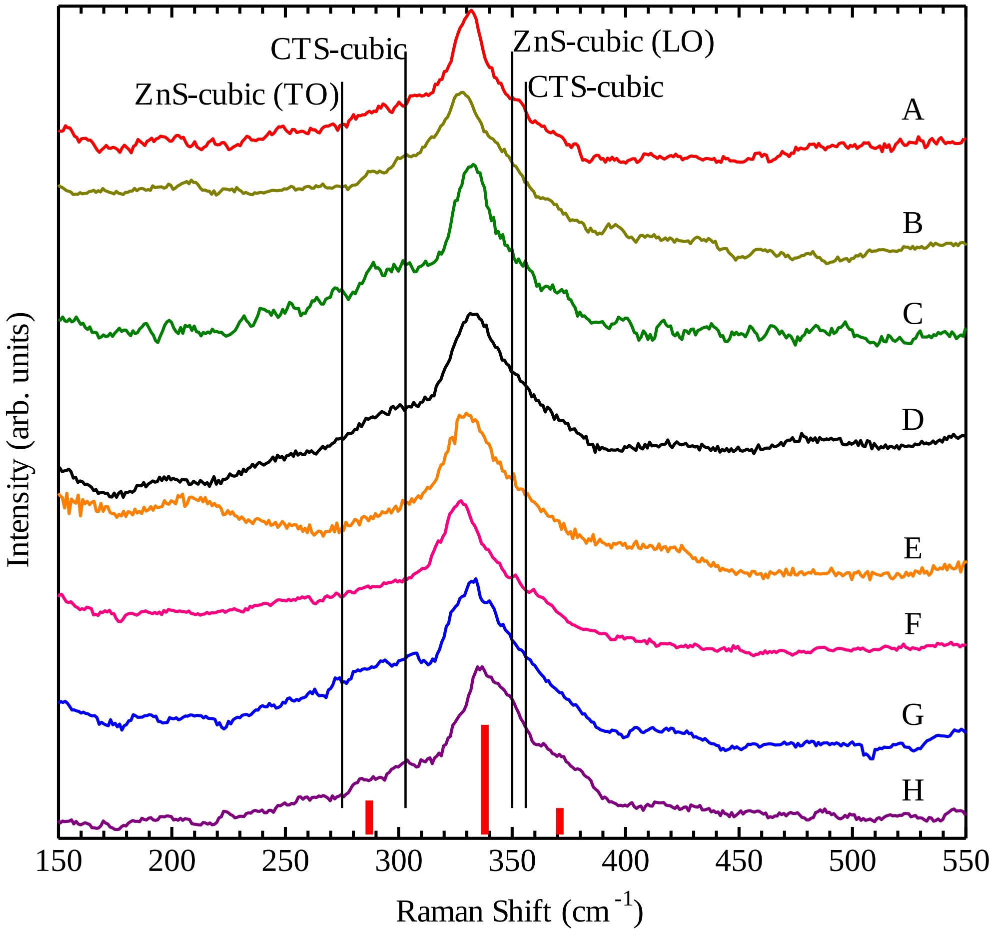
CTS-cubic
ZnS-cubic (TO)
ZnS-cubic (LO)
CTS-cubic
A
B
C
D
E
F
G
H
Intensity (arb. units)
150
200
250
300
350
400
450
500
550
Raman Shift (cm^{-1})

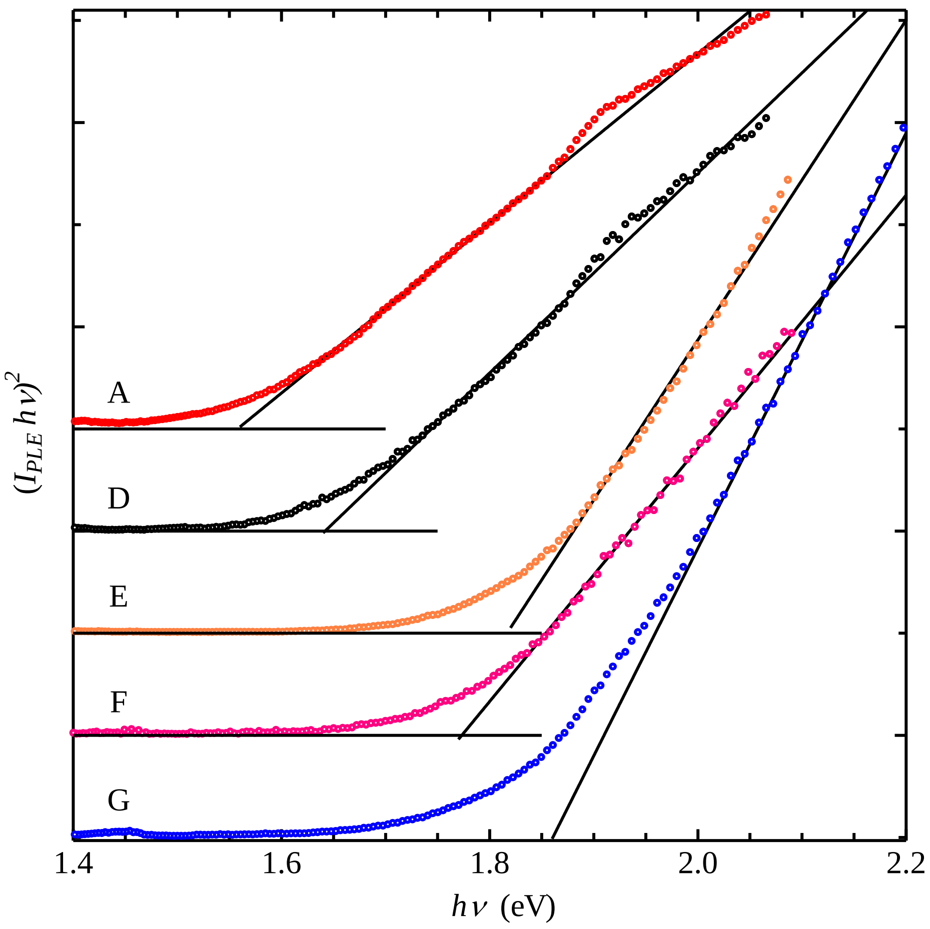
A
D
E
F
G
$(I_{PLE}\,h\nu)^2$
1.4
1.6
1.8
2.0
2.2
$h\nu$ (eV)

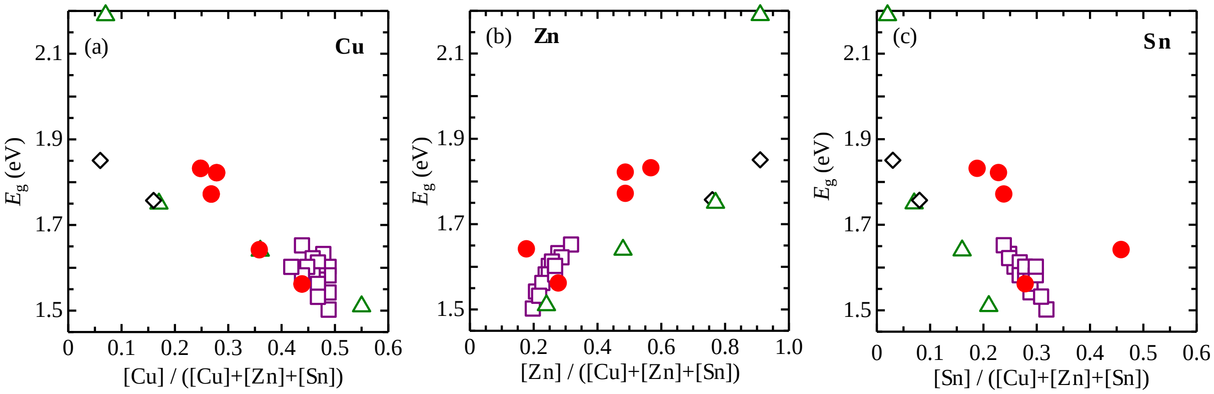
(a)
Cu
E_g (eV)
2.1
1.9
1.7
1.5
0
0.1
0.2
0.3
0.4
0.5
0.6
[Cu] / ([Cu]+[Zn]+[Sn])
(b)
Zn
E_g (eV)
2.1
1.9
1.7
1.5
0
0.2
0.4
0.6
0.8
1.0
[Zn] / ([Cu]+[Zn]+[Sn])
(c)
Sn
E_g (eV)
2.1
1.9
1.7
1.5
0
0.1
0.2
0.3
0.4
0.5
0.6
[Sn] / ([Cu]+[Zn]+[Sn])